INTERNATIONAL JOURNAL FOR NUMERICAL METHODS IN FLUIDS
Int. J. Numer. Meth. Fluids 2004; **45**:1137–1159 (DOI: 10.1002/fld.733)

Simulation of single- and two-phase flows on sliding unstructured meshes using finite volume method

B. Basara[1,*,†], A. Alajbegovic[2] and D. Beader[3]

[1]*AVL List GmbH, Hans List Platz 1, Graz A-8020, Austria*
[2]*Powertrain Engineering, Inc., 47519 Halyard Dr., Plymouth, MI 48170-2438, U.S.A.*
[3]*AVL AST, Stegne 21, Ljubljana SI-1521, Slovenia*

SUMMARY

The paper presents an efficient finite volume method for unstructured grids with rotating sliding parts composed of arbitrary polyhedral elements for both single- and two-phase flows. Mathematical model used in computations is based on the ensemble averaged conservation equations. These equations are solved for each phase and in case of single-phase flow reduce to the transient Reynolds-averaged Navier–Stokes (TRANS) equations. Transient flow induced by rotating impellers is thus resolved in time. The use of unstructured grids allows an easy and flexible meshing for the entire flow domain. Polyhedral cell volumes are created on the arbitrary mesh interface placed between rotating and static parts. Cells within the rotating parts move each time step and the new faces are created on the arbitrary interfaces only, while the rest of the domain remain 'topologically' unchanged. Implicit discretization scheme allows a wide range of time-step sizes, which further reduce the computational effort. Special attention is given to the interpolation practices used for the reconstruction of the face quantities. Mass fluxes are recalculated at the beginning of each time step by using an interpolation scheme, which enhances the coupling between the pressure and velocity fields. The model has been implemented into the commercially available CFD code AVL SWIFT (AVL AST, SWIFT Manual 3.1, AVL List GmbH, Graz, Austria, 2002). Single-phase flow in a mixing vessel stirred by a six-bladed Rushton-type turbine and two-phase flow in aerated stirred vessel with the four-blade Rushton impeller are simulated. The results are compared with the available experimental data, and good agreement is observed. The proposed algorithm is proved to be both stable and accurate for single-phase as well as for the two-phase flows calculations.

KEY WORDS: Reynolds-averaged Navier–Stokes equations; finite volume method; sliding meshes; two-phase flow

1. INTRODUCTION

There are several important practical applications with rotating geometries in the fluid domain. Here is presented a numerical method for the treatment of rotation within the frame of unstructured grids, both for single-phase and two-phase flows. Although it is applied to the

*Correspondence to: B. Basara, AVL List GmbH, Hans List Platz 1, Graz A-8020, Austria.
†E-mail: branislav.basara@avl.com

Published online 14 May 2004
Received 21 June 2003
Revised 7 March 2004

motion of rotating impellers in stirred tanks, the method itself is generic and can be used for other applications with rotating elements.

Flow simulation in stirred tanks attracted considerable interest in the recent past. Several studies of single-phase flows in stirred tanks were presented. Luo *et al.* [1] performed calculations of the mixing in the baffled stirred vessel using the technique that allowed the cells to shear and slide to accommodate relative motion on a structured grid. Tabor *et al.* [2] used the same method together with the multiple reference frame (MRF) approach to simulate the mixing case with the Rushton turbine by Wu and Patterson [3]. The MRF approach approximates the rotation by implementing body forces within the rotating part and is primarily suitable for steady-state simulations. The results obtained by Tabor *et al.* [2] reported good agreement with the data using the MRF approach.

More recently, Lilek *et al.* [4] extended the multi-block structured grid approach to take into account arbitrary interfaces by mixing two data structures. Regular indexing was employed within the structured grid while an additional table was used to store faces along the sliding interface. In this way, the implicit nature of the solution method was ensured as the block interface is not treated as an additional boundary. Wechsler *et al.* [5] also used the multi-block structured grid approach, together with MRF where the stator and rotor were calculated in two different reference frames, rotating and fixed. Their method is practical from the computational perspective, but limited to the block-structured grids where all cells have to be within vertices forming hexahedral volumes. Even more important, the observed solution accuracy was not very good. Nevertheless, the concept of multiple frame of reference has been explored in many studies due to the possibility of performing low cost steady-state calculations. On the other hand, the method becomes impractical for transient calculations or when the rotation is combined with the translation.

Numerical modelling of two-phase flows in mixing vessels represents considerably increase in difficulty with respect to single-phase flow modelling. Issa [6] presented the results of the two-phase flow simulation in the mixing vessel at steady state using the MRF approach. Ranade [7, 8] developed a computational snapshot approach for simulating the flow in a stirred vessel. The method consists of modelling of the suction and ejection of the fluid from the back and front sides of the impeller blades as mass sources. In this way, it is possible to simulate the impeller motion while maintain static mesh. Ljungquvist and Rasmuson [9] performed simulations of solid/liquid two-phase flows in an axially stirred vessel. The simulations were based on multi-block structured grid approach using the two-fluid model. The rotation of the six-blade impeller was modelled using the impeller boundary condition method. As a result, only steady-state conditions could be simulated. Ljungquvist and Rasmuson were primarily interested in the modelling of solid/liquid flows and tested several different momentum interfacial exchange models and compared the results to the experimental data, while here is presented the development and validation of the sliding grid numerical scheme for unstructured meshes.

The focus of the work presented herein is to perform highly accurate transient calculations using the algorithm optimized for rotating geometries and unstructured grids. Such an approach is more expensive computationally, when compared to the methods presented in the before mentioned references. However, as the computing time reduces with the continuous increase of the computing power, this is less and less of an issue.

The use of unstructured grids with polyhedral cell elements significantly reduces the meshing effort. On the negative side, numerical codes running unstructured meshes are less suitable

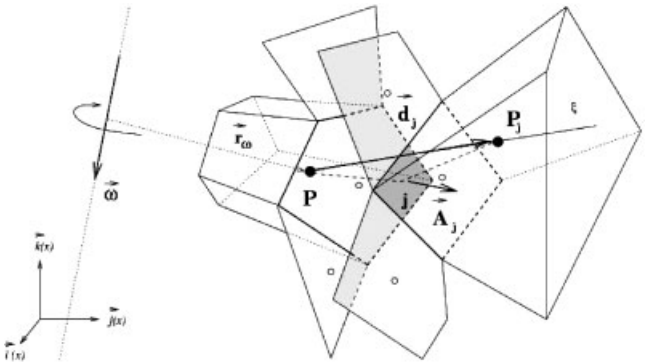

Figure 1. Calculation volumes and an arbitrary interface.

for parallel computing. Numerical practices for computational fluid dynamics (CFD) on such meshes require reformulation of the data structure, interpolation procedures and discretization of convective terms, which is often a difficult task. However, when it comes to dynamic grid modifications caused by movement or by adaptive grid refinement, such algorithms have unprecedented advantages over conventional 'structured' solvers. Sliding mesh applications fall into such a category, and can be handled with considerably more efficiency than by using flow solvers that cannot accommodate polyhedral cell volumes.

Finite volume method is well suited for the discretization procedures on unstructured grids [10–12]. The key feature of the approach presented here is the definition of connectivity between the cell faces and cell centres, shown in Figure 1. The connectivity provides for each face the two neighbouring cell centres sharing this same face. Using such definition of connectivity, the face fluxes are being calculated by a single sweep over all the faces in the mesh. The faces created on the arbitrary interfaces can have arbitrary number of vertices. The cell volumes in the proximity of an arbitrary interface may also result in an arbitrary number of faces. However, in the calculation they are treated in the same way as the cells not adjacent to the arbitrary interface. This enormously simplifies meshing of the complete computational domain. The parts of the domain not moving or moving at a different speed are meshed separately. They are connected through arbitrary interfaces and then re-connected each new time step. The cells next to the interface might change the number of faces exceeding the six. As a result, interpolation practices for the calculation of variables and their gradients on the faces are the key to a successful discretization scheme.

The purpose of the paper is primarily to present a numerical method that can be used for the simulation of rotating geometries. The models used have to be adequate enough to allow comparison with the experimental data. Therefore, the mathematical model used for the simulation of both single-phase and two-phase flows is presented first. The model is based on the two-fluid modelling and in case of single-phase flow reduces to the standard RANS formulation. Detailed description of the numerical techniques used in the discretization of the model follows. Special focus is devoted to the treatment of the sliding interface.

Finally, calculation results are presented both for single- and two-phase flow cases. Single-phase flow computations are compared with the experimental results for the stirred vessel configuration provided by Wu and Patterson [3]. They used a simple cylindrical tank equipped

with four stationary flow deflectors/baffles and stirred by a six-bladed Rushton-type turbine. The test case used for the validation of the two-phase flow calculations is the aerated stirred vessel with the four-blade Rushton impeller and four stationary baffles. The experimental data were obtained by Bombač *et al.* [13] and consist of detailed air volume fraction measurements. The objective of the present study is to assess the accuracy of the fully unstructured algorithm applied to sliding grids and adopted for the two-fluid model in Euler–Euler frame.

2. MATHEMATICAL MODEL

Mathematical model is presented from the perspective of the multifluid model, which is used to describe multiphase flows [14, 15]. The multifluid model is obtained through the ensemble averaging of the conservation equations. In the case of single-phase flows, the model reduces to the well-known Reynolds-averaged Navier–Stokes equations. In a multi-phase flow case, the phases are distinguished by the volume fraction, α_n, which is a measure of the fraction of the volume filled by the phase n. The evolution of volume fraction is described by the following equation:

$$\frac{\partial \alpha_n \rho_n}{\partial t} + \nabla \cdot \alpha_n \rho_n \mathbf{v}_n = 0, \quad n = 1, \ldots, N \tag{1}$$

which represents the mass conservation of the phase n. The quantities in the equations are the phase n density, ρ_n, and its velocity, $\mathbf{v}_n$. N is the number of phases. The compatibility condition has to be satisfied:

$$\sum_{n=1}^{N} \alpha_n = 1 \tag{2}$$

In the single-phase case, N equals one. The momentum conservation equation equals

$$\frac{\partial \alpha_n \rho_n \mathbf{v}_n}{\partial t} + \nabla \cdot \alpha_n \rho_n \mathbf{v}_n \mathbf{v}_n = -\alpha_n \nabla p + \nabla \cdot \alpha_n (\boldsymbol{\tau}_n + \mathbf{T}_n^t) + \alpha_n \rho_n \mathbf{g} + \sum_{l=1, l \neq n}^{N} \mathbf{M}_{nl}, \quad n = 1, \ldots, N \tag{3}$$

where $\mathbf{g}$ is the gravity vector, $\mathbf{M}_{nl}$, represents the momentum interfacial interaction between phases n and l, and p is pressure. Pressure is assumed equal for all phases:

$$p_n = p, \quad n = 1, \ldots, N \tag{4}$$

The main purpose of the paper is to present a numerical method for the handling of sliding interfaces in both single- and two-phase flows. The purpose is not to develop and present a physical model for the processes that occur in mixing flows. However, in order to verify the method against the experimental data, some comprehensive models need to be used. In the present case, the implemented interfacial momentum source for the interaction between phases n and l includes drag and turbulent dispersion force [16]:

$$\mathbf{M}_{nl} = C_{\mathrm{D}} \frac{1}{8} \rho_n A_i''' |\mathbf{v}_{\mathrm{r}}| \mathbf{v}_{\mathrm{r}} + C_{\mathrm{TD}} \rho_n k_n \nabla \alpha_n = -\mathbf{M}_{ln} \tag{5}$$

k_n is turbulence kinetic energy for phase n, and $\mathbf{v}_{\mathrm{r}}$ is relative velocity between phases l and n:

$$\mathbf{v}_{\mathrm{r}} = \mathbf{v}_l - \mathbf{v}_n \tag{6}$$

C_{TD} is turbulence dispersion coefficient. We used the value of 0.1 as suggested by Lahey *et al.* [17]. The interfacial area density, A_i''', is modelled following References [18, 19]:

$$A_i'''=\frac{6\alpha_{gs}}{D_b}\frac{1-\alpha_g}{1-\alpha_{gs}}$$

$$\alpha_{gs}=\begin{cases}\alpha_g & \alpha_g<0.25\\ 0.3929-0.57142\alpha_g & 0.25\leqslant\alpha_g<0.6\\ 0.05 & \alpha_g\geqslant 0.6\end{cases} \tag{7}$$

where α_g is the volume fraction of gas (air), and D_b is the mean bubble diameter. The bubble diameter value used in the calculations was 1mm. Reasonable agreement with the experimental data was obtained using this bubble diameter value. This value might not match the true bubble size in the experiment. Any discrepancy between the actual and used bubble sizes is primarily due to the model deficiencies. Considerable effort is still necessary to improve the interfacial interactions models. However, it is not the intention of the present work to present the contribution to the modelling, but to provide an efficient numerical technique.

Drag coefficient, C_D, is dominating the interactions between the two phases and as a result the volume fraction distribution. The correlation by Ishii and Zuber [20] distinguishes between different interactions through the entire volume fraction span (and different flow regimes) and is therefore chosen for the calculations:

$$C_D=\begin{cases}\frac{2}{3}D_B\sqrt{\frac{g(\rho_l-\rho_g)}{\sigma}}\left(\frac{1+17.67(1-\alpha_g)^{1.238}}{18.67(1-\alpha_g)^{1.5}}\right)^2 & \alpha_g\leqslant 0.25\\ 9.8(1-\alpha_g)^3 & \alpha_g>0.25\end{cases} \tag{8}$$

where σ is surface tension, ρ_l is liquid density and ρ_g is gas (air) density. The phase n shear stress, $\boldsymbol{\tau}_n$, equals

$$\boldsymbol{\tau}_n=\mu_n(\nabla\mathbf{v}_n+\nabla\mathbf{v}_n^T) \tag{9}$$

μ_n is molecular viscosity. Reynolds stress, $\mathbf{T}_n^t$, is defined as

$$\mathbf{T}_n^t=-\rho_n\overline{\mathbf{v}_n'\mathbf{v}_n'} \tag{10}$$

The correlations $\overline{\mathbf{v}_n'\mathbf{v}_n'}$, known as the Reynolds stresses, are additional unknowns in this set of equations, which leave the number of unknowns larger than the number of equations. In the k–ε eddy-viscosity model, the Reynolds stresses are evaluated from the Bousinessq's assumption, given by

$$\mathbf{T}_n^t=-\rho_n\overline{\mathbf{v}_n'\mathbf{v}_n'}=\mu_n^t(\nabla\mathbf{v}_n+\nabla\mathbf{v}_n^T)-\frac{2}{3}\rho_n k_n\mathbf{I} \tag{11}$$

Turbulent viscosity, μ_n^t, is modelled as

$$\mu_n^t=\rho_n C_\mu\frac{k_n^2}{\varepsilon_n} \tag{12}$$

Table I. Closure coefficients in the k–ε model.

σ_k	σ_ε	C_1	C_2	C_μ
1.0	1.3	1.44	1.92	0.09

In order to close the k–ε model, it is necessary to solve equations for the turbulent kinetic energy, k, and its dissipation rate, ε:

$$\frac{\partial \alpha_n \rho_n k_n}{\partial t} + \nabla \cdot \alpha_n \rho_n \mathbf{v}_n k_n = \nabla \cdot \alpha_n \left(\mu_n + \frac{\mu_n^t}{\sigma_k} \right) \nabla k_n + \alpha_n P_n - \alpha_n \rho_n \varepsilon_n + \sum_{l=1, l \neq n}^{N} K_{nl}, \quad n = 1, \ldots, N \tag{13}$$

$$\frac{\partial \alpha_n \rho_n \varepsilon_n}{\partial t} + \nabla \cdot \alpha_n \rho_n \mathbf{v}_n \varepsilon_n = \nabla \cdot \alpha_n \left(\mu_n + \frac{\mu_n^t}{\sigma_\varepsilon} \right) \nabla \varepsilon_n + \alpha_n C_1 P_n \frac{\varepsilon_n}{k_n} - \alpha_n C_2 \rho_n \frac{\varepsilon_n^2}{k_n} + \sum_{l=1, l \neq n}^{N} D_{nl}, \quad n = 1, \ldots, N \tag{14}$$

These equations are valid for incompressible flows considered in this study. K_{nl} and D_{nl} are the interfacial exchange terms between the phases n and l in the turbulent kinetic energy and dissipation equations, respectively. Contribution of the interfacial terms in both equations is neglected. Even though turbulence is undoubtedly affected by the interfacial effects, its contribution is of the second order with respect to the interfacial terms in the momentum equation.

The production term due to shear, P_n, for the phase n is equal to

$$P_n = \mathbf{T}_n^t : \nabla \mathbf{v}_n \tag{15}$$

The closure coefficients from turbulence kinetic energy and dissipation equations are provided in Table I.

In the present study, single-phase and multi-phase flow calculations were performed in conjunction with standard wall functions. The standard wall function is applied by introducing the wall turbulent viscosity, thus

$$\mu_{n,w} = \frac{y_{n,P}^+}{\mathrm{v}_{n,P}^+} \mu_n \tag{16}$$

where

$$\mathrm{v}_{n,P}^+ = \begin{cases} y_{n,P}^+ & \text{if } y_{n,P}^+ < 11.63 \\ \dfrac{1}{\kappa} \ln(E y_{n,P}^+) & \text{if } y_{n,P}^+ \geqslant 11.63 \end{cases} \tag{17}$$

where κ is the von Karman constant ($\kappa = 0.41$) and E is the logarithmic profile constant that depends on the surface roughness. In our calculations we used the value of 9.0. The non-dimensional wall distance is given as

$$y_{n,P}^{+} = \frac{\rho_n C_\mu^{1/4} k_n^{1/2} \delta}{\mu_n} \tag{18}$$

where δ denotes the normal distance from the near-wall node to the wall. The flux of turbulent kinetic energy at the wall is taken to be zero, a condition simply enforced by setting the appropriate finite-difference coefficients to zero. The values of the turbulent kinetic energy, k, at the node closest to the wall is therefore obtained from the solution of its equation there. Single modification to the standard equation is required: it affects the way in which the rate of production of k is evaluated at the grid nodes closest to the wall. Dissipation rate ε is fixed for the first-to-wall cells by assuming that turbulence is in local equilibrium.

In case of single-phase flow, the above equations reduce to the following set of Reynolds-averaged Navier–Stokes equations with the turbulence closure terms described above:

$$\frac{\partial \rho \mathbf{v}}{\partial t} + \nabla \cdot \rho \mathbf{v}\mathbf{v} = -\nabla p + \nabla \cdot (\boldsymbol{\tau} + \mathbf{T}^t) + \rho \mathbf{g} \tag{19}$$

$$\frac{\partial \rho k}{\partial t} + \nabla \cdot \rho \mathbf{v} k = \nabla \cdot \left(\mu + \frac{\mu^t}{\sigma_k} \right) \nabla k + P - \rho \varepsilon \tag{20}$$

$$\frac{\partial \rho \varepsilon}{\partial t} + \nabla \cdot \rho \mathbf{v} \varepsilon = \nabla \cdot \left(\mu + \frac{\mu^t}{\sigma_\varepsilon} \right) \nabla \varepsilon + C_1 P \frac{\varepsilon}{k} - C_2 \rho \frac{\varepsilon^2}{k} \tag{21}$$

3. NUMERICAL PROCEDURE

The discretization of the governing differential equations is obtained using a cell-centred finite volume approach. In the method used here, the governing equations are integrated, term-by-term, over the 'polyhedral' control volumes such as the one shown in Figure 1. Such discretization practices have been recently explored in other publications, e.g. Demirdzic *et al.* [11], Marthur and Marthy [12] and others. The method has been applied and proven on various applications. It is based on the integral form of the generic conservation law. Thus, for the moving control volume with the outward surface (cell-face) vectors, all modelling equations can be described as

$$\underbrace{\frac{\partial}{\partial t} \int_V \alpha_n \rho_n \phi_n \, \mathrm{d}V}_{\text{Rate of change: } R} + \underbrace{\int_A \alpha_n \rho_n (\mathbf{v}_n - \mathbf{v}_S) \phi_n \, \mathrm{d}\mathbf{A}}_{\text{Convection: } C}$$

$$= \underbrace{\int_A \alpha_n \boldsymbol{\Gamma}_{\phi,n} \cdot \nabla \phi_n \, \mathrm{d}\mathbf{A}}_{\text{Diffusion: } D} + \underbrace{\int_A \alpha_n \mathbf{q}_{\phi,n}^A \, \mathrm{d}\mathbf{A} + \int_V \left(\alpha_n q_{\phi,n}^V + \sum_{l=1, l \neq n}^{N} \mathrm{S}_{\phi,nl} \right) \mathrm{d}V}_{\text{Sources: } S} \tag{22}$$

where a general variable $\phi_n(x_k, t)$ can represent either scalars or vector and tensor field components of the phase n. Here, the Cartesian co-ordinate system (x, y, z) with the unit vectors $(\mathbf{i}, \mathbf{j}, \mathbf{k})$ is used and tensor notation is employed. In Equation (22) ρ_n is fluid density, t is time, $\mathbf{v}_n$ is the fluid velocity vector, $\mathbf{v}_S$ is the velocity of the moving control volume, $\mathbf{\Gamma}_{\phi,n}$ is the diffusion coefficient for the variable ϕ, $q^V_{\phi,n}$ and $\mathbf{q}^A_{\phi,n}$ are the volumetric and surface source terms, respectively. Again, the index n denotes the phase.

In the present method, all dependent variables are stored at the geometric centre of cells. Two implicit differencing schemes can be used to evaluate the rate of change: the first-order accurate Euler and second-order accurate three time level scheme [21]. In order to calculate surface integrals over faces of arbitrary-shaped cells (see Figure 1) and account for them in Equation (22), one can choose to loop over all faces. This approach requires the face-based connectivity, i.e. for each internal face j defined by the surface vector $\mathbf{A}_j$ (that points out from the cell P to P_j) the indices of adjacent cells P and P_j should be known.

Both surface and volume integrals are approximated by the values in geometric centre of the face or cell. This single point quadrature (mid-point rule) is a second-order accurate approximation and leads to the following semi-discrete control volume equation:

$$\frac{\mathrm{d}}{\mathrm{d}t}(\alpha_{n,P}\rho_{n,P}\phi_{n,P}V_P) + \sum_{j=1}^{n_f} C_{n,j} - \sum_{j=1}^{n_f} D_{n,j} = \sum_{j=1}^{n_f} (\mathbf{q}^A_{n,\phi}\cdot\mathbf{A})_j + \left(q^V_{n,\phi} + \sum_{l=1,\, l\neq n}^{N} \mathrm{S}_{\phi,nl}\right)_P V_P \tag{23}$$

where $C_{n,j}$ and $D_{n,j}$ are phase-n convective and diffusion transport through the face j, are defined as

$$C_{n,j} = \dot{m}_{n,j}\phi_{n,j} \tag{24}$$

$$D_{n,j} = \alpha_{n,j}(\mathbf{\Gamma}_{\phi,n})_j \cdot (\nabla\phi_n)_j \cdot \mathbf{A}_j \tag{25}$$

n_f is the number of cell faces. Face mass fluxes, $\dot{m}_{n,j}$, are defined as

$$\dot{m}_{n,j} = \alpha_{n,j}\rho_{n,j}(\mathbf{v}_{n,j}\cdot\mathbf{A}_j - \dot{V}_j) \tag{26}$$

$$\dot{V}_j = \mathbf{v}_{S,j}\cdot\mathbf{A}_j \tag{27}$$

where $\dot{V}_j$ is the volume flux, i.e. the volume swept by a cell face during its movement with the face velocity $\mathbf{v}_{S,j}$. The mass fluxes must satisfy the phase-n continuity equation, which now reads

$$\frac{\partial}{\partial t}(\alpha_{n,P}\rho_{n,P}V_P) + \sum_{j=1}^{n_f} \dot{m}_{n,j} = 0 \tag{28}$$

At the same time, the mixture mass conservation has to be satisfied as well:

$$\sum_{n=1}^{N}\left(\frac{\partial}{\partial t}(\alpha_{n,P}\rho_{n,P}V_P) + \sum_{j=1}^{n_f}\dot{m}_{n,j}\right) = 0 \tag{29}$$

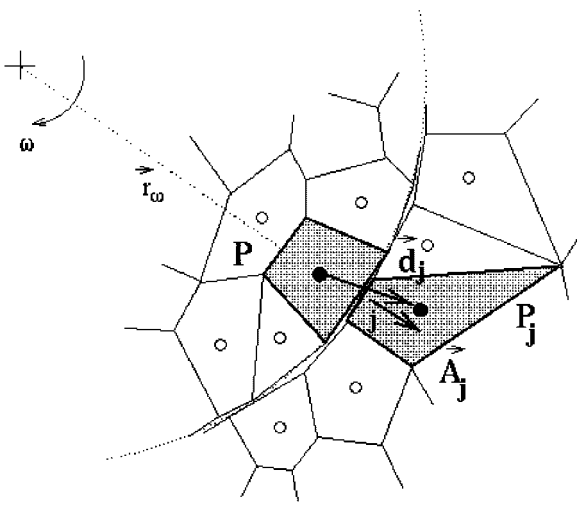

Figure 2. Two unstructured blocks (e.g. moving and non-moving) before the connection through the arbitrary interface into a single calculation domain.

In the case of single-phase flows, both Equations (28) and (29) reduce into the following equation:

$$\frac{\partial}{\partial t}(\rho_P V_P) + \sum_{j=1}^{n_f} \dot{m}_j = 0 \tag{30}$$

Space (or volume) conservation law (SCL) can be cast into the following form [4]:

$$\frac{\partial}{\partial t}\int_{V_P} \mathrm{d}V - \sum_{j=1}^{n_f} \dot{V}_j = 0 \tag{31}$$

For the sliding cases considered in the paper, the moving face velocity is recalculated from the face-centre positions or from the given radial velocity, and the surface vectors as well as calculation volumes inside rotating part remain constant. As a result, the space conservation law is satisfied. However, small inconsistencies may appear at the interface between the moving and non-moving parts, (see Figure 2). If we assume that the part with point P moves and part with point P_j does not, then the faces between them may look as shown in Figure 2 before the connection. Intersecting these faces and finding the common face shared by both volumes with centres P and P_j, will result in volume change on one of the sides. Therefore, it is recommended that the moving surface or the faces of the moving volumes is the referent surface. This means that the faces from non-moving cells are projected onto this surface to create new common faces, which ensure that the moving volumes will remain unchanged. As a result, Equation (31) will be definitely satisfied. We should have in mind that the starting blocks, as these shown in Figure 2, are kept until the end of calculation to calculate the grid positions at two successive time steps. Assuming that the velocity vector is normal to the surface vector at the shared faces of the arbitrary interface, the values $\mathbf{v}_{S,j} \cdot \mathbf{A}_j$ for these faces are set to be exactly zero. The volumes of the cells in the static part do not change, only

the volumes next to the arbitrary interface and the faces at the arbitrary interface should be recalculated.

Intensive use of the arbitrary interface requires accurate interpolation practices for the calculation of the cell-face values and their gradients. With the use of linear interpolation, the cell-face values are calculated as

$$\phi_j = f_j \phi_p + (1 - f_j)\phi_{p_j} \tag{32}$$

where $f_j = |\mathbf{r}_{P_j} - \mathbf{r}_j|/(|\mathbf{r}_{P_j} - \mathbf{r}_j| + |\mathbf{r}_j - \mathbf{r}_P|)$ is the cell-face interpolation factor. In such case, that the vector connecting two centres P and P_j does not pass through the face centre, additional correction may be introduced [11], thus

$$\phi_j = \phi_{j'} + \nabla\phi_{j'} \cdot (\mathbf{r}_j - \mathbf{r}_{j'}) \tag{33}$$

where linear interpolation given by Equation (32) is used to obtain $\phi_{j'}$ and $\nabla\phi_{j'}$. The point j' can be defined to be the mid-point between cell centres P and P_j. With that, $f_j = 0.5$ and $\mathbf{r}_j - \mathbf{r}_{j'}$ is easily recalculated. For the convective transport in Equation (24), the second-order MINMOD scheme is used for the cell-face values as proposed by Przulj and Basara [22].

The simplest approach for the calculations of the cell gradients is to use the Gauss' Theorem, thus

$$\nabla\phi_p = \frac{1}{V_p} \sum_{j=1}^{n_f} \phi_j \mathbf{A}_j \tag{34}$$

Other authors recommend a linear least-square approach [10, 23]. Using Gauss' Theorem and with the use of simple mathematical reconstruction to replace vertex values only with the contributions from cells P and P_j, one can derive the following formula for the cell-face gradient:

$$\nabla\phi_j = \overline{\nabla\phi_j} + \frac{\mathbf{A}_j}{\mathbf{A}_j \cdot \mathbf{d}_j}[(\phi_{Pj} - \phi_P) - \overline{\nabla\phi_j} \cdot \mathbf{d}_j] \tag{35}$$

where $\mathbf{d}_j$ is the distance vector between P and P_j, see Figure 1. The interpolated face gradient $\overline{\nabla\phi_j}$ can be calculated either by linear interpolation or by arithmetic averaging.

After introducing the above interpolation practices into the balance Equation (22), the outcome is a set of algebraic equations: one for each control volume and for each transport equation. An algebraic equation can be written concisely as

$$a_P \phi_P = \sum_{j=1}^{n_f} a_j \phi_{P_j} + S_\phi \tag{36}$$

where n_f is the number of internal cell faces; a_P and a_j are coefficients and S_ϕ is the source term. Thus, for a computational domain with M control volumes, a system of $M \times N$ algebraic equations needs to be solved for N dependent variables ϕ. Considering the non-linearity and coupling of equations, they are solved by the segregated SIMPLE-like algorithm of Patankar and Spalding [24] (see also References [11, 21]). Each equation for the given variable is decoupled by treating other variables as known, which leads to a sub-set of M linear algebraic equations for each dependent variable. The linearized algebraic equations are solved by very efficient, preconditioned conjugate gradient methods. The symmetric gradient method is used

to solve equations with the symmetric matrix and the biconjugate method (Bi-CGSTAB) of Van der Vorst [25] for equations with an asymmetric matrix. Both methods are used with an incomplete Cholesky preconditioning technique (see Reference [26]).

The SIMPLE algorithm effectively couples the velocity and pressure fields by converting a discrete form of the continuity equation into an equation for the pressure correction. The pressure corrections are then used to update the pressure and velocity fields so that the velocity components obtained from the solution of momentum equations satisfy the continuity equation. On non-staggered grids, a special interpolation practice is required for the face velocities, Rhie and Chow [27] and Ferziger and Peric [21]. By manipulating the discretized momentum equations using Equation (35) expressed in a vector form, one can arrive at the following formula for the face velocity vector:

$$\mathbf{v}_{n,j} = \overline{\mathbf{v}}_{n,j} - \overline{\left(\frac{\alpha_{n,P} V_P}{a_{n,P}}\right)_j (\nabla p_j - \overline{\nabla p_j})} \tag{37}$$

After replacing the pressure gradient ∇p_j by the face gradient given by Equation (35), the face velocity can be calculated as

$$\mathbf{v}_{n,j} = \overline{\mathbf{v}}_{n,j} - \frac{1}{2}\left(\frac{\alpha_{n,P} V_P}{a_{n,P}} + \frac{\alpha_{n,P_j} V_{P_j}}{a_{n,P_j}}\right) \frac{\mathbf{A}_j}{\mathbf{A}_j \cdot \mathbf{d}_j} \left[(p_{P_j} - p_P) - \frac{1}{2}(\nabla p_{P_j} + \nabla p_P) \cdot \mathbf{d}_j\right] \tag{38}$$

Calculations on different grids with different differencing schemes are prerequisite for reliable simulations. As shown above, all terms are discretized with at least second-order accuracy. All the calculations were performed on fine numerical grids. Furthermore, error estimation was used to assess grid quality. Its description follows.

The error based on one-dimensional analysis of convective and normal-diffusion terms was considered as proposed by Muzaferija and Gosman [28]. The variation of variable ϕ and its gradients in direction ξ (see Figure 1) which connects two neighbouring points is analysed. Therefore, the third-order polynomial variation of ϕ along ξ and its gradient projected in the direction of d_j can be written as

$$\tilde{\phi}_j = C_0 + C_1 \xi_j + C_2 \xi_j^2 + C_3 \xi_j^3 \tag{39}$$

$$\nabla \phi_j \frac{d_j}{|d_j|} = C_1 + 2C_2 \xi_j + 3C_3 \xi_j^2 \tag{40}$$

Now, the convection and diffusion fluxes over faces can be obtained as

$$\tilde{C}_j = \tilde{F}_j \tilde{\phi}_j \quad \text{and} \quad \tilde{D}_j = -\lambda_{\phi_j} \left(\nabla \phi_j \frac{d_j}{|d_j|}\right) \frac{d_j}{|d_j|} A_j \tag{41}$$

Furthermore, the constants $C_{i=1,3}$ are defined to satisfy the following boundary conditions (see Figure 1), for detailed information see original reference [28], thus:

$$\begin{aligned} &\underline{\xi = 0}; \quad \phi = \phi_P; \quad (\nabla \phi)^{\xi} = (\nabla \phi)_P^{\xi} \\ &\underline{\xi = |d_j|}; \quad \phi = \phi_{P_j}; \quad (\nabla \phi)^{\xi} = (\nabla \phi)_{P_j}^{\xi} \end{aligned} \tag{42}$$

Comparing fluxes given by Equation (41) with the fluxes used in the calculations, the error can be defined as

$$\tau_P = \sum_{j=1}^{n_f} [(\tilde{C}_j - C_j) + (\tilde{D}_j - D_j^{\text{normal-diffusion}})] \tag{43}$$

Normalized error τ_P is then used for leading the process of grid refinements. Note that this discretization error should be considered only when the iteration error is very small. Also, note that the cross diffusion is not taken into account. However, the method is very efficient to analyse the discretization error by using a single grid.

The model has been implemented into the commercially available CFD code AVL SWIFT [29] which is then used for all the calculations presented in the paper.

4. RESULTS AND DISCUSSION

4.1. Single-phase flow case—six blade Rushton mixer

The test case chosen for the single-phase flow calculations is a simple mechanically driven mixer stirred by a 6-bladed Rushton-type turbine in a cylindrical vessel equipped with 4 stationary flow deflectors/baffles. Details of geometry are available in the original paper of Wu and Patterson [3], see Figure 3 for the flow configuration. The diameter of the tank was 0.270 m and a turbine was placed $\frac{1}{3}$ of the diameter from the base of the tank. Measured data is available in the impeller stream and in the near region around the impeller, and at the planes 0° and 45° with respect to the baffle planes. The impeller speeds were 100, 200 and 300 rpm. The results of the laser Doppler anemometry are provided as mean values taken over 6 different stations. Here is considered the case with the impeller speed of 200 rpm.

The grid used was the result of the 'error' optimization, see Equation (43). It was found that the largest error was in the cells next to the arbitrary interface and therefore they had to be refined. Step-by-step improvement of three different grids lead to the final grid with the size of 339 504 cells (see Figure 3). This is a considerably finer grid compared to the one used by Wechsler *et al.* [5] for the similar case and for the transient calculations. The influence of time step was also analysed. Three different time steps have been used, namely 2.5, 5.0 and 7.5 ms corresponding to the 3, 6 and 9° swept by the impeller within each time step, respectively. The results for the three time steps were very similar, as were the convergence rates. However, the smallest time step was used to calculate the results for the comparison with the experimental data, as the results obtained in such way are deemed to be the most accurate.

Figure 4 shows the predicted pressure at five radial monitoring locations in the mid-baffle plane at $\theta = 45°$ for $z = 0$. A captured period corresponds to approximately 20 time steps of simulation time. This means 0.05 s (20×2.5 ms) of the real time corresponding to 60° sweep, being exactly the time needed for the impeller blades to pass the same point in the flow.

Figures 5–7 show the radial, tangential and axial normalized velocity profiles in the mid baffle plane at different radial positions, r: 0.05, 0.06, 0.07, 0.077, 0.09 and 0.105 m. The best agreement between the experimental data and the calculations is observed close to the impeller. Some discrepancies are visible further away from the impeller on both sides in the axial direction. The same can be observed for the different radial positions at the same height, z.

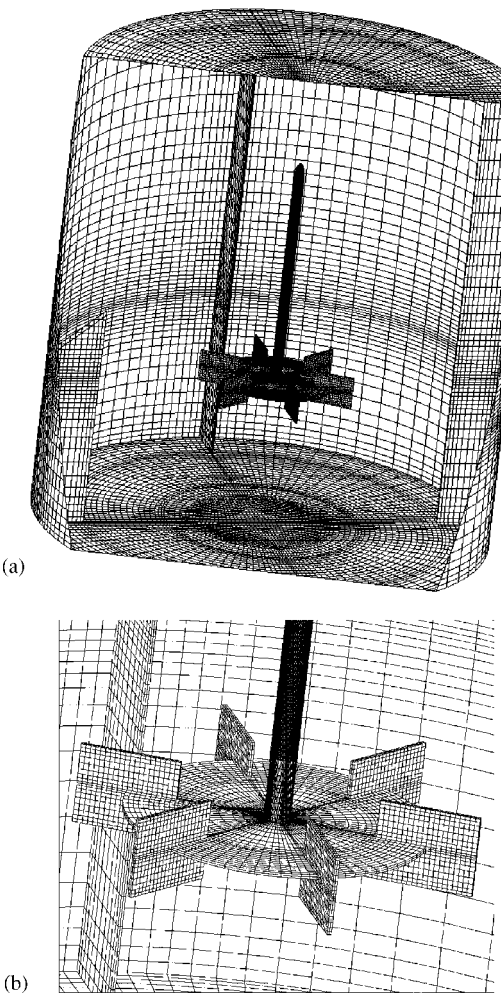

Figure 3. Computational grid for the six-blade Rushton impeller mixer (a) and impeller details (b).

Predicted maximum values of the radial velocity are overestimated at the furthermost positions. The same applies for the tangential component. The axial component is better captured below than above the impeller at all positions. Overall, the shape of profiles is well predicted. It appears that the standard k–ε model can be blamed for the over-predicted turbulence kinetic energy and that part of the error due to its isotropic formulation. Better results can be expected by using more accurate turbulence models, e.g. second-moment closures. However, the predicted turbulence kinetic energy at the plane $z = 0$ presented in Figure 8, shows that the turbulence model might especially influence the mixing of the departing flow from the impeller zone. Nevertheless, the smooth distribution of the turbulence kinetic energy through the arbitrary interface marked with the black line in Figure 8, illustrates the general accuracy of the interpolation practices used for the convection, diffusion, and all cell-face values

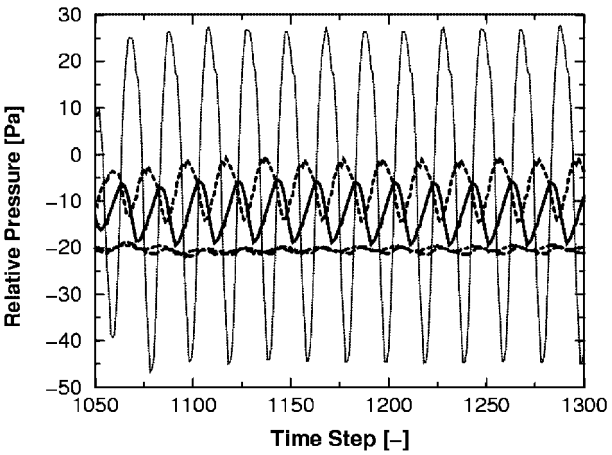

Figure 4. Calculated pressure at different monitoring locations (.... $r = 6$ cm, --- $r = 7$ cm, ___ $r = 7.7$ cm, _ _ $r = 9$ cm, -.-.- $r = 10.5$ cm).

needed in the numerical solution scheme. The convergence rate for all equations within the single time step is shown in Figure 9. The residuals decrease monotonically confirming the robustness of the numerical procedure. It should be pointed out that the peak in residuals at the first iteration of each time step is avoided by using Equation (38) to recalculate face velocities (have in mind that convection fluxes at the interface between rotor and stator are lost after each movement). This means that some computing time has to be spent for the reconstruction of terms in Equation (38).

4.2. Two-phase flow case—four blade Rushton mixer

The experimental data of Bombač *et al.* [13] were used for the validation of the two-phase flow simulations in a mixer with sliding grids. Bombač *et al.* performed detailed air volume fraction measurements using the conductivity probe. Vessel used in the experiments had the diameter of 0.45 m and the height of 0.49 m. The geometry can be seen in Figure 10. The mesh consisted of 77 712 cells. Figure 10(a) shows the surface discretization of the whole geometry. The details of the mesh for the impeller part are shown in Figure 10(b). Four blades with the area $0.038\ \text{m} \times 0.03\ \text{m}$ were mounted at a distance 0.056 m from the axis of rotation. All the geometry measurements are provided in the original paper by Bombač *et al.* [13].

The experiments were done at two impeller speeds—265.8 and 376 rpm. Two different bubble injection methods were used—annular and ring sparger. Impeller speed of 265.8 rpm and ring sparger is considered for the validation. The inlet velocity of air, based on the provided mass flux of $1.67 \times 10^{-3}\ \text{m}^3/\text{s}$ and ring sparger inlet area of $4.524 \times 10^{-4}\ \text{m}^2$, is 3.7 m/s. No water was allowed to enter through the sparger, therefore its velocity was set to zero. The flow field was initialized with water level at 0.45 m as reported by Bombač *et al.* [13]. Pressure of 1 bar was prescribed at the top boundary. Both water and air properties ware taken at temperature 25°C. Simulation was performed in transient mode with 1 ms time step. Calculated were 3900 time steps, which yield approximately 4 s of the simulated real

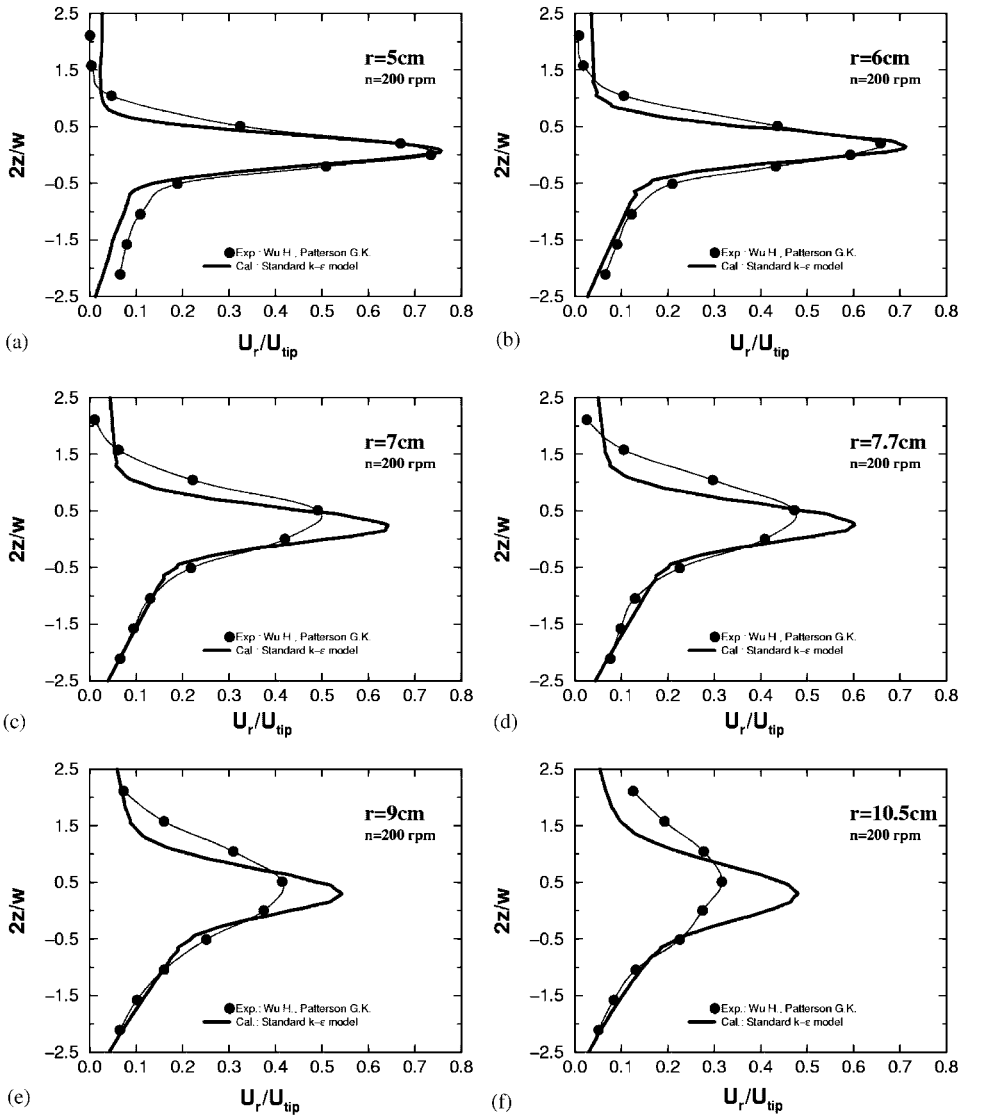

Figure 5. Radial normalized velocity profiles along the main axis at six different radial positions: (a) $r = 0.05$ m; (b) $r = 0.06$ m; (c) $r = 0.07$ m; (d) $r = 0.077$ m; (e) $r = 0.09$ m; and (f) $r = 0.105$ m.

time and 17 complete rotations of the impeller. Computer with Intel single processor running at 2.6 GHz and Linux operating system was used as a computational platform. The simulation took 13 days of CPU time.

The key feature of the presented numerical method is the capability to perform transient calculations in flows with rotating parts. The radially integrated volume fractions at three different axial positions as a function of time are shown in Figure 11. It can be seen that

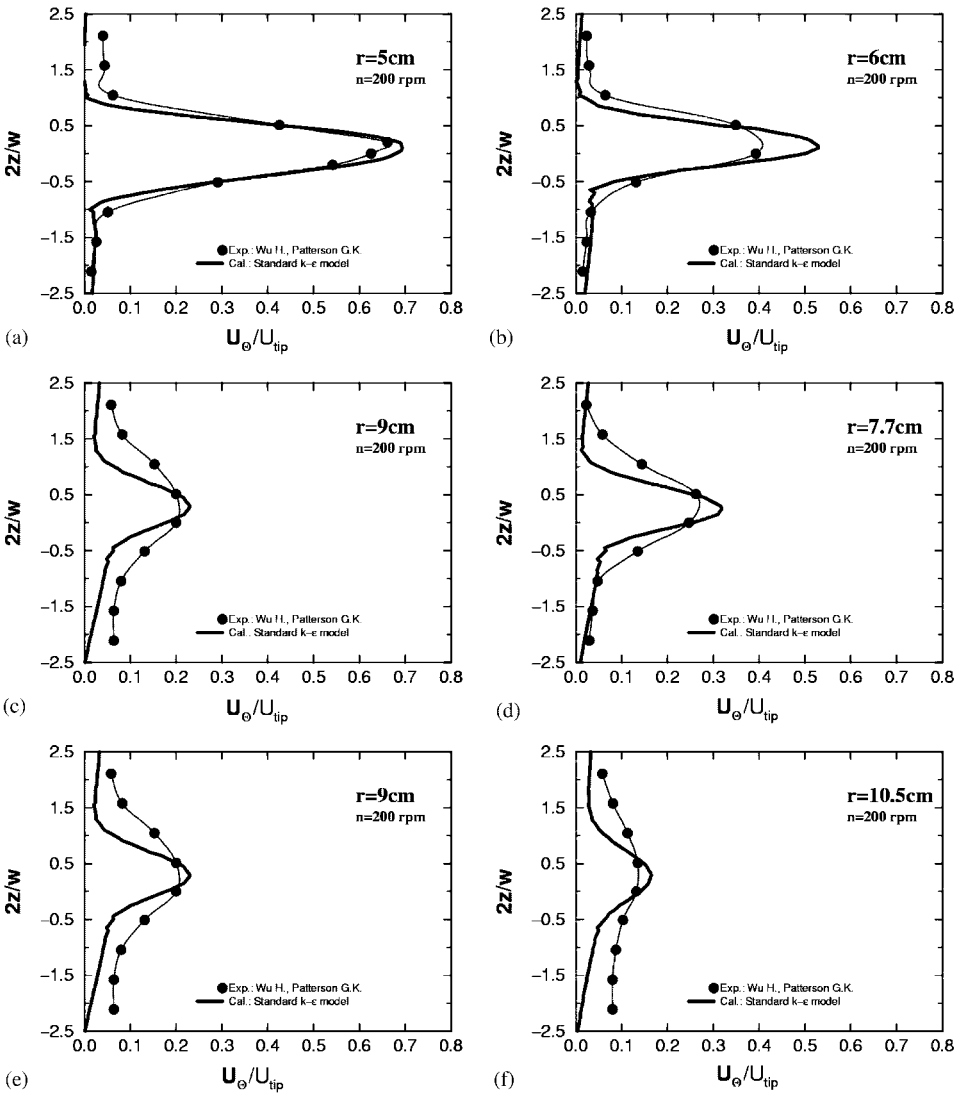

Figure 6. Tangential normalized velocity profiles along the main axis at six different radial positions: (a) $r = 0.05$ m; (b) $r = 0.06$ m; (c) $r = 0.07$ m; (d) $r = 0.077$ m; (e) $r = 0.09$ m; and (f) $r = 0.105$ m.

the steady-state conditions are reached approximately 2 s after the initial transient. Slight oscillations persist after that. The largest amplitude in oscillations is observed at $z = 0.15$ m, approximately at the height of the impeller. The snapshots of the air volume fraction field on the vessel symmetry plane at six different times are shown in Plate 1. Two major directions of the air motion can be observed. Part of the injected air moves straight up from the inlet sparger. The other part is being sucked into the low-pressure region around the impeller. Buoyancy force is pushing air upward at the same time. As a result, the air spreads around

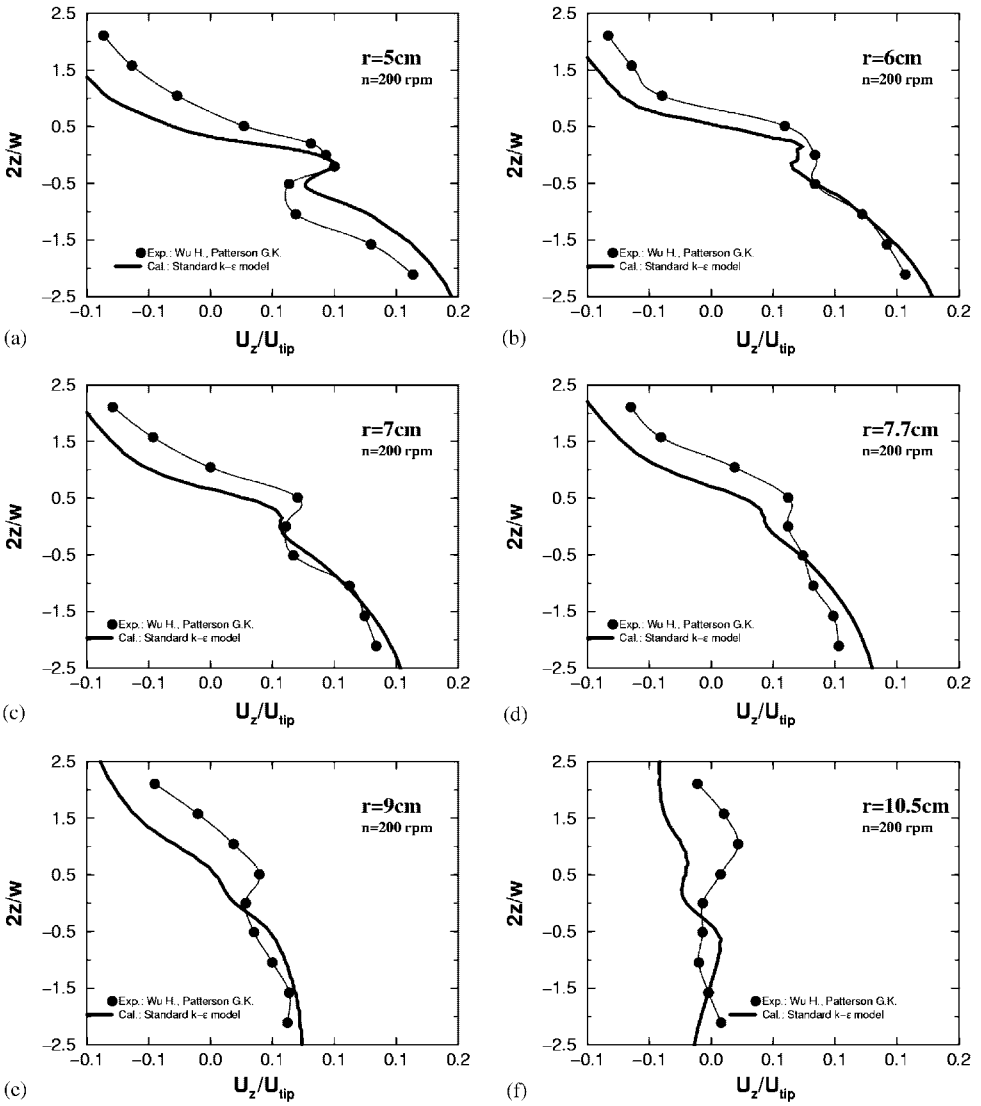

Figure 7. Axial normalized velocity profiles along the main axis at six different radial positions: (a) $r = 0.05$ m; (b) $r = 0.06$ m; (c) $r = 0.07$ m; (d) $r = 0.077$ m; (e) $r = 0.09$ m; and (f) $r = 0.105$ m.

the vessel, mixes with the water, and then moves upward towards the outlet. The evolution of volume fraction fields at different times is in agreement with time-dependent behaviour shown in Figure 11. It can be noted that the 'steady' state is reached after 2 s. There is almost no difference between the snapshots at times 2 and 2.5 s.

The comparison of calculated and measured data obtained at steady conditions were performed by averaging the calculated values from time $t = 2$ s to the end of the calculation.

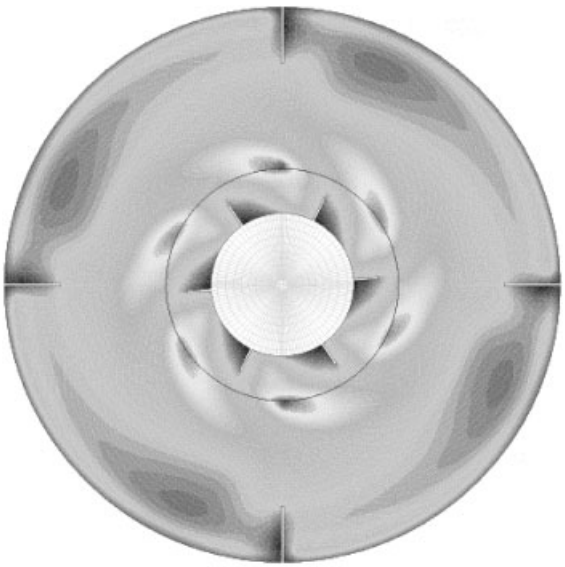

Figure 8. Predicted turbulence kinetic energy by the standard k–ε model. The arbitrary interface is marked with the black line.

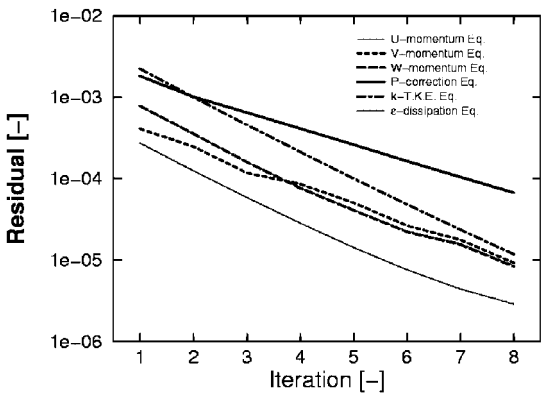

Figure 9. Convergence rate in one time step for the single-phase flow case at the time step 1450 ($t = 7.55$ s).

Spatial evolution of air volume fraction as a function of the axial position and radial position $r = 0.092$ m is shown in Figure 12. Substantial agreement between the experimental data and calculated values can be noticed up to the height of 0.15 m. At higher axial positions the predicted volume fraction levels are considerably less than measured. This is due to higher air diffusion rates in the experiment, which are caused by the deficiencies of the interfacial momentum exchange models used in the calculations.

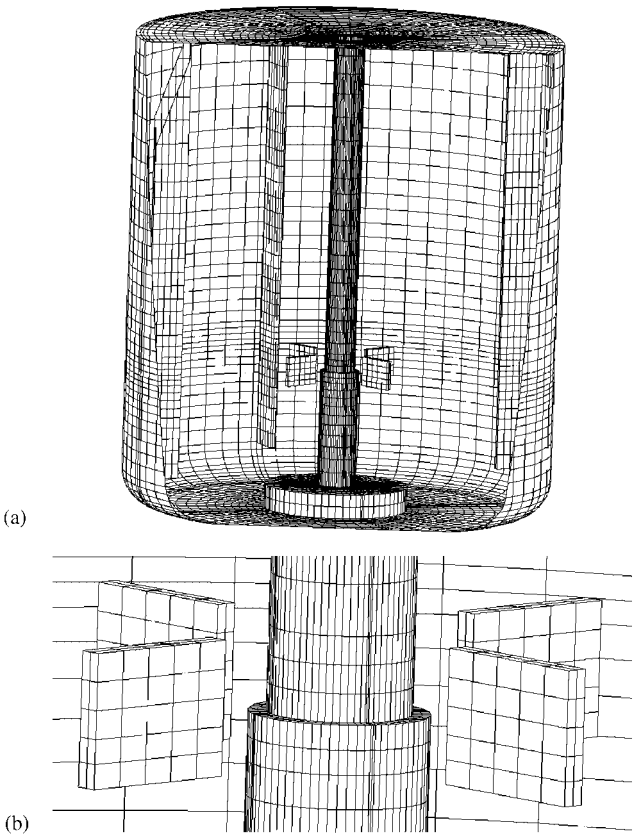

Figure 10. Computational grid (77712 internal cells) for the four-blade Rushton impeller mixer: (a) entire geometry; and (b) impeller details.

Comparison between the measured and calculated radially integrated air volume fraction values as a function of the axial position is shown in Figure 13. Again, the agreement is good at low axial positions, while considerably higher volume fraction levels can be observed in the experiment between $z = 0.2$ and 0.3. Measured is more air entrainement in the high recirculation region around the impeller than predicted in the calculations. This is again due to the deficiencies of the momentum interfacial exchange model. It can be assumed that the drag between air and water is too low in the calculation resulting in exceedingly high relative velocities and therefore faster escape of air from the vessel. Still, the overall trend of the calculated results is in agreement with the experimental data as can be seen in Figures 12 and 13.

The lateral air volume fraction distribution on the plane at $z = 0.15$ m is shown in Plate 2(a). The rotation of the impeller is in clockwise direction. The structure can be recognized as the $L33$ structure and was observed by Bombač *et al.* [13] for this case. The $L33$ structure is characterized by the large air cavities behind the impeller blades. Lateral turbulence kinetic energy distribution shown on the same plane for both water and air can

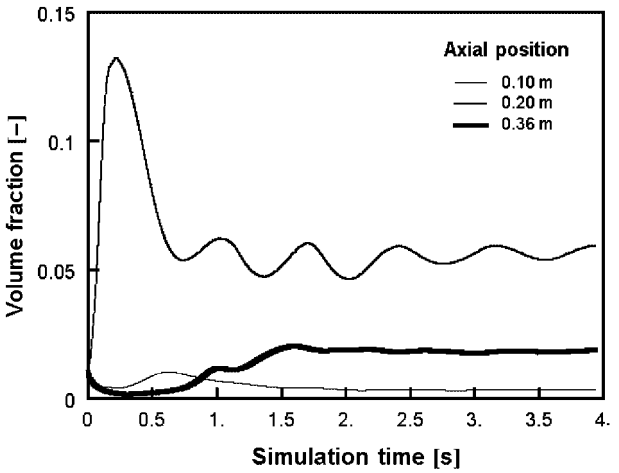

Figure 11. Radially integrated volume fraction at three different axial positions as a function of simulation time.

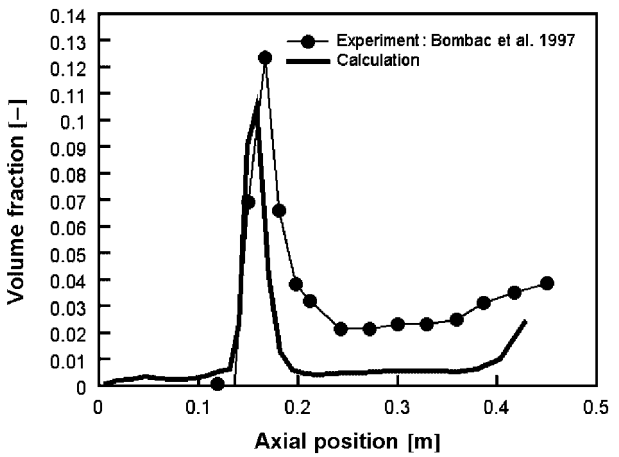

Figure 12. Comparison between the measured and calculated volume fractions at the radial position 0.092 m as a function of axial position.

be seen in Plates 2(b) and 2(d), consecutively. It can be noted that the arbitrary interface is seamlessly integrated into the calculation. The same lateral air turbulence kinetic energy distribution shown from a different perspective can be seen in Plate 2(c).

The convergence rate for pressure correction, x velocity component, turbulence kinetic energy, turbulence dissipation and volume fraction equations within the single time step for the two-phase flow calculation is shown in Figure 14. Similarly as for the single-phase flow case, the residuals decrease monotonically confirming the robustness of the numerical procedure.

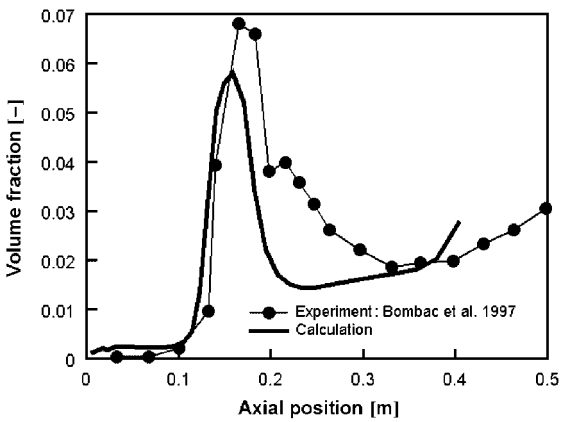

Figure 13. Comparison between the measured and calculated radially integrated volume fractions as a function of axial position.

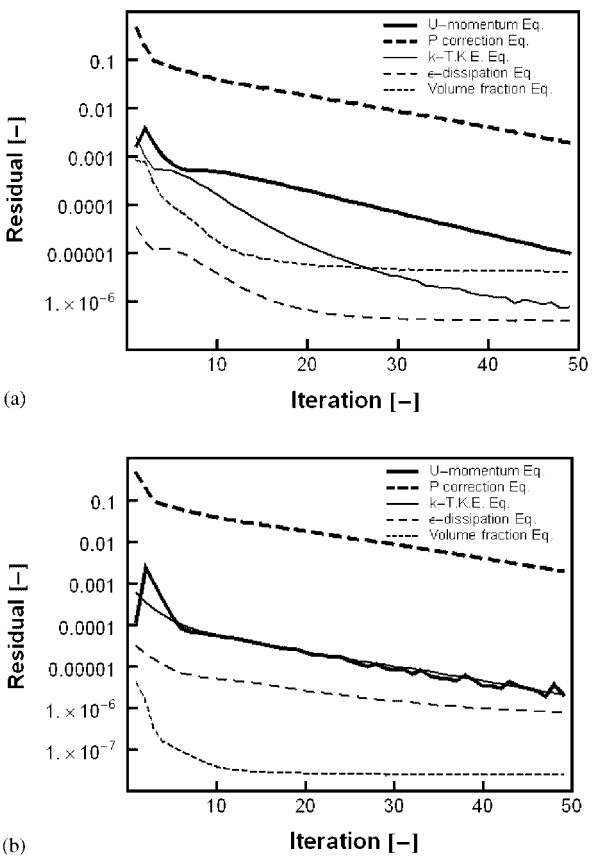

Figure 14. Convergence rate in one time step for the two-phase flow case at the time step 1900 ($t = 1.837$ s): (a) water; and (b) air.

5. CONCLUSIONS

The main conclusion drawn from this study is that the numerical procedure made for the universal polyhedral calculation volumes can be extended straightforwardly for the sliding mesh applications with no special modifications. Due attention should be given to the definition of the referent surface before its connection with the arbitrary interface. In this way, the space conservation law is automatically fulfilled. Therefore, there is no need for additional enforcement of the SCL during calculations, except that the new volumes of the cells next to the arbitrary interface and in the static part have to be recalculated. Further validation of the two-phase flow simulations would require velocity measurements together with volume fraction data. New experiments by [30] using computer-automated radioactive particle tracking (CARPT) together with volume fraction measurements with computer tomography [31] seem very promising for future validation of the two-phase flow simulations in stirred tanks. Nevertheless, the presented method was shown to be robust and reasonably accurate for both single-phase and two-phase flow calculations.

REFERENCES

1. Luo JY, Gosman AD, Issa RI, Middleton JC, Fitzgerald MK. Full flow field of mixing in baffled stirred vessels. *Proceedings of the Institution of Chemical Engineers Research Event*, Birmingham, UK, 1993.
2. Tabor G, Gosman AD, Issa RI. Numerical simulation of the flow in a mixing vessel stirred by a Rushton turbine. *Proceedings of the Institution of Chemical Engineers Research Event*, Birmingham, UK, 1993.
3. Wu H, Patterson GK. Laser-Doppler measurements of turbulent-flow parameters in stirred mixer. *Chemical Engineering Science* 1989; **44**:2207–2221.
4. Lilek Z, Muzaferija S, Peric M, Seidl V. Computations of unsteady flows using non-matching blocks of structured grid. *Numerical Heat Transfer Part B* 1997; **32**:403–418.
5. Wecshler K, Breuer M, Durst F. Steady and unsteady computations of turbulent flows induced by a 4/45° pitched-blade impeller. *Journal of Fluids Engineering* 1999; **121**:318–329.
6. Issa RI. Numerical modelling of two-phase flow in mixing vessels. *Fourth European Computational Fluid Dynamics Conference*, Athens, Greece, 1998.
7. Ranade VV. An efficient computational model for simulating flow in stirred vessels: a case of Rushton turbine. *Chemical Engineering Science* 1997; **52**:4473–4484.
8. Ranade VV. CFD Predictions of flow near impeller blades in baffled stirred vessels: assessment of computational snapshot approach. *Chemical Engineering Communications* 2002; **189**:895–922.
9. Ljungquvist M, Rasmuson A. Numerical simulation of the two-phase flow in an axially stirred vessel. *Transactions of the Institution of Chemical Engineers* 2001; **79**:533–546.
10. Barth TJ. Aspects of unstructured grids and finite-volume solvers for the Euler and Navier–Stokes equations. *Computational Fluid Dynamics*, Lectures Series 1994-05, von Karman Institute for Fluid Dynamics, 1994.
11. Demirdzic I, Muzaferija S, Peric M. Computation of turbulent flows in complex geometries. In Tzabiras GD (ed.), *Calculation of complex turbulence flows*. Ch. 7. WIT Press: Southampton, 1999.
12. Marthur SR, Murthy JY. All speed flows on unstructured meshes using a pressure correction approach. *AIAA Paper* 1999-3365, 1999.
13. Bombač A, Žun I, Filipič B, Žumer M. Gas-filled cavity structures and local void fraction distribution in aerated stirred vessel. *A.I.Ch.E. Journal* 1997; **43**:2921–2931.
14. Drew DA, Passman SL. *Theory of Multicomponent Fluids*. Springer: New York, 1998.
15. Ishii M. *Thermo-Fluid Dynamics Theory of Two-Phase Flow*. Eyrolles: Paris, 1975.
16. Lopez de Bertodano M. Turbulent bubbly two-phase flow in a triangular duct. *Ph.D. Thesis*, Rensselaer Polytechnic Institute, Troy, New York, 1992.
17. Lahey RT Jr, Lopez de Bertodano M, Jones OC. Phase distribution in complex geometry conduits. *Nuclear Engineering and Design* 1993; **141**:177–201.
18. Kurul N, Podowski MZ. On the modelling of multidimensional effects in boiling channels. *ANS Proceedings*, *National Heat Transfer Conference*, Minneapolis, Minnesota, 1991.
19. Anglart H, Andersson S, Podowski MZ, Kurul N. An analysis of multidimensional void distribution in two-phase flows. *6th International Topical Meeting on Nuclear Reactor Thermal Hydraulics*, Nureth-6, Grenoble, France, 1993.

20. Ishii M, Zuber N. Drag coefficient and relative velocity in bubbly, droplet or particulate flows. *A.I.Ch.E. Journal* 1979; **25**:843–855.
21. Ferziger JH, Peric M. *Computational Methods for Fluid Dynamics*. Springer: New York, 1996.
22. Przulj V, Basara B. Bounded convection schemes for unstructured grids. *AIAA Paper* 2001-2593, Anaheim, USA, 2001.
23. Muzaferija S. Adaptive finite volume method for flow predictions using unstructured meshes and multigrid approach. *Ph.D. Thesis*, Imperial College, University of London, UK, 1994.
24. Patankar SV, Spalding DB. A calculation procedure for heat, mass and momentum transfer in three-dimensional parabolic flows. *International Journal of Heat and Mass Transfer* 1972; **15**:1510–1520.
25. Van der Vorst HA. Bi-CGSTAB: a fast and smoothly converging variant of Bi-CG for the solution of nonsymmetric linear system. *SIAM Journal on Scientific Computing* 1992; **13**:631–644.
26. Meijerink JA, van der Vorst HA. Guidelines for the usage of incomplete decompositions in solving sets of linear equations as they occur in practical problems. *Journal of Computational Physics* 1981; **44**:134–155.
27. Rhie CM, Chow WL. Numerical study of the turbulent flow past an airfoil with trailing edge separation. *AIAA Journal* 1983; **21**:1525–1532.
28. Muzaferija S, Gosman D. Finite-volume CFD procedure and adaptive error control strategy for grids of arbitrary technology. *Journal of Computational Physics* 1997; **138**:766–787.
29. AVL AST, SWIFT Manual 3.1, AVL List GmbH, Graz, Austria, 2002.
30. Rammohan AR, Kemoun A, Al-Dahhan MH, Dudukovic MP. A Lagrangian description of flows in stirred tanks via computer-automated radioactive particle tracking (CARPT). *Chemical Engineering Science* 2001; **56**: 2629–2639.
31. Rammohan AR. Gas-liquid flow in stirred tank reactor. *Proceedings—Chemical Reaction Engineering Laboratory Annual Meeting*, Washington University, St Louis, Missouri, USA, 2002.

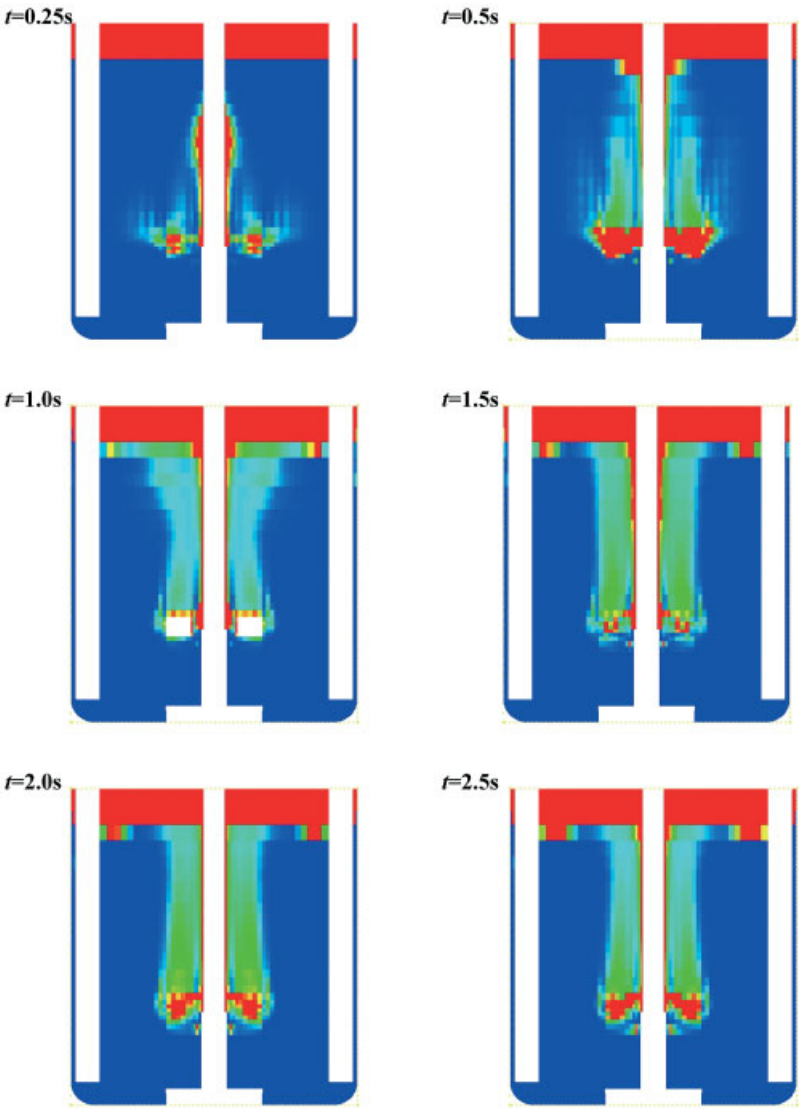

Plate 1. The evolution of air volume fraction on the symmetry plane as a function of simulation time, t.

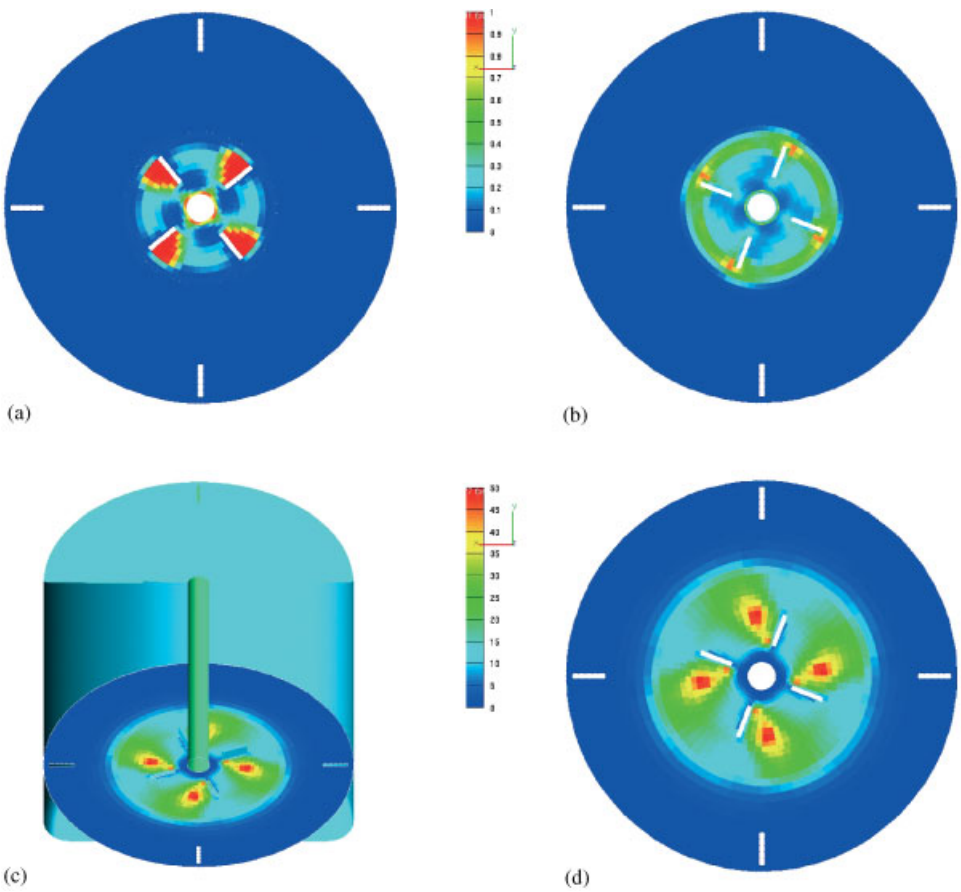

Plate 2. Different quantities displayed on the plane at the axial position 0.15 m: (a) air volume fraction; (b) water turbulence kinetic energy; (c) and (d) air turbulence kinetic energy shown at two different perspectives.